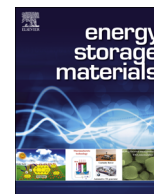




ELSEVIER

Contents lists available at ScienceDirect

Energy Storage Materials

journal homepage: www.elsevier.com/locate/ensm

Carbothermic reduction synthesis of red phosphorus-filled 3D carbon material as a high-capacity anode for sodium ion batteries



Jie Sun^a, Hyun-Wook Lee^b, Mauro Pasta^c, Yongming Sun^a, Wei Liu^a, Yanbin Li^a, Hye Ryoung Lee^a, Nian Liu^a, Yi Cui^{a,d,*}

^a Department of Materials Science and Engineering, Stanford University, Stanford, CA 94305, USA

^b School of Energy and Chemical Engineering, Ulsan National Institute of Science and Technology (UNIST), Ulsan 44919, Korea

^c Department of Materials, University of Oxford, 16 Parks Road, Oxford OX1 3PH, UK

^d Stanford Institute for Materials and Energy Sciences, SLAC National Accelerator Laboratory, 2575 Sand Hill Road, Menlo Park, CA 94025, USA

ARTICLE INFO

Article history:

Received 27 April 2016

Accepted 27 April 2016

Available online 28 April 2016

Keywords:

Red phosphorus

Three dimensional structure

Carbothermic reaction

Sodium-ion batteries

ABSTRACT

Phosphorus is an attractive negative electrode material for sodium ion batteries due to its high theoretical specific capacity of 2596 mA h g^{-1} . However, it suffers poor conductivity ($10^{-12} \text{ S m}^{-1}$), slow reaction dynamics, and large volume expansion ($\sim 440\%$) during the sodiation process, leading to rapid capacity decay upon cycling. Great attention has been devoted to improving the electrical conductivity via mixing phosphorus particles with conductive carbon materials, yet little emphasis has been placed on addressing the volume expansion issue, which may leads to the loss of electrical contact between the active material and the current collector, and the sequent deterioration of the overall electrochemical performance. Here, we demonstrate a carbothermic reduction method to fabricate ultrafine red phosphorus particles ($\sim 10 \text{ nm}$) embedded in a three-dimensional carbon framework, in which numerous interconnected nanopores are generated accompanied by the carbonization of polyethylene glycol. During discharge/charge processes, nanosized phosphorus particles accommodate the large stress without cracking, and decrease the diffusion length, as well as connect strongly with carbon framework, resulting in an improved conductivity, a reversible specific capacity of 1027 mA h g^{-1} (at 0.2 C) and high capacity retention of 88% over 160 cycles.

© 2016 Published by Elsevier B.V.

1. Introduction

Growing energy needs and depletion of fossil-fuel resources demand the pursuit of sustainable energy alternatives, including both renewable energy sources and sustainable storage technologies. Therefore, it is essential to consider material abundance, eco-friendly synthetic processes and performance when designing new electrochemical storage systems. Sodium ion batteries (SIBs) have recently received a lot of attention as a low-cost and environmentally friendly alternative to lithium ion batteries (LIBs), [1–3] due to the ready availability of sodium resources and the similar chemistry of sodium and lithium ions [4,5]. Although SIB and LIB share many technical similarities in cathodes and electrolytes, [6–8] adapting LIB anode materials to SIBs has revealed an unsuccessful strategy. The representative example is the Li–Si alloy anode, which can store 4.4 Li per Si, and deliver a specific capacity

of 4200 mA h g^{-1} [9]. However, Si cannot be electrochemically sodiated, in spite of the existence of Na–Si alloys [10]. Moreover, it is also difficult to find crystalline host anode materials for Na-ion insertion reaction partially because of the large diameter of Na (2.04 \AA) compared to Li (1.52 \AA). For example, Na ions cannot be intercalated into the two-dimensional layered graphite [11].

Phosphorus (P) electrochemically reacts with Na to form Na_3P , and delivers a theoretical specific capacity of 2596 mA h g^{-1} , [12] which is much higher than other anode candidates, such as germanium ($\text{Na}_{15}\text{Ge}_4$, 369 mA h g^{-1}), [13] tin ($\text{Na}_{15}\text{Sn}_4$, 847 mA h g^{-1}), [14] lead ($\text{Na}_{15}\text{Pb}_4$, 485 mA h g^{-1}), [15] and antimony (Na_3Sb , 660 mA h g^{-1}) [16]. Moreover, red P is earth-abundant and non-toxic. However, it is synthesized industrially starting from the toxic and very reactive white P, it suffers from a poor electrical conductivity ($10^{-12} \text{ S m}^{-1}$) [17] and has a large volume expansion ($\sim 440\%$) during the sodiation process, leading to rapid capacity decay upon cycling. To improve the electrical conductivity, commercial phosphorus particles have been mixed with various carbon materials, [18–24] such as, carbon black, [19–21] carbon nanotubes and [22,23] grapheme [24]. However, there is little success on

* Corresponding author at: Department of Materials Science and Engineering, Stanford University, Stanford, CA 94305, USA.

E-mail address: yicui@stanford.edu (Y. Cui).

solving the other problem i.e. the large volume expansion upon sodiation, similarly as Si anode for LIBs, [25,26] which leads to the loss of electrical contact of active materials and deterioration of the electrochemical performance upon cycling.

In order to simultaneously solve the problems of the poor conductivity, large volume expansion and harmful synthesis process, herein, we demonstrate a synthesis strategy of carbothermic reduction of P_4O_{10} into P, resulting in embedding red P nanoparticles in a three-dimensional (3D) carbon framework (P/C composite). Such a design has multiple advantages: (1) The resulting, ultrafine red P particles, with a diameter of ~ 10 nm, not only minimize the diffusion distance of sodium ions, but also allow for a favorable accommodation of the large volume changes without the fracturing that can occur in bulk or micron-sized materials. (2) Red P particles are electrically connected to the conductive 3D carbon framework via P–O–C bonds: the carbon framework functions as an electrical highway and a mechanical backbone, so that all the red P particles are electrochemically active. (3) The interlinked channels are easily filled with electrolyte, thus facilitating the transportation of a large flux of Na ions. (4) A scalable and bottom-up method is applied to fabricate the designed structure, by which P_4O_{10} is the substitute for the toxic white P.

2. Materials and methods

2.1. Synthesis of P/C composite

P_4O_{10} and polyethylene glycol (PEG) (MW, ~ 1500) were purchased from Sigma-Aldrich. Firstly, solid PEG transformed into liquid by heating at 80°C in a vacuum oven. White powdered P_4O_{10} (2.5 g) was added into the above liquid PEG (7.5 g). After 40 min at 80°C in the vacuum oven, its color changed to black because the super absorbent P_4O_{10} extracted the water from PEG and polymerized to a long chain molecule of polyphosphoric acid, meanwhile the PEG was carbonized by losing H_2O . Subsequently, the intermediate products were transferred into an alundum boat (Fisher Scientific) and calcined at 900°C with a ramping rate of $15^\circ\text{C}/\text{min}$ and an argon flow rate of 5 sccm (Standard Cubic Centimeter per Minute) under sunlight. When some red substance appeared onto the inner wall of the quartz tube (about 0.5 h at

900°C), the boat was moved to the 250°C zone in the quartz tube and remained for 1 h under sunlight (Supplementary information, Fig. S1). The low temperature (250°C) was carried out to condense the produced red P, according to its melting point of 590°C . Sunlight catalyzes the production of red P instead of the toxic and flammable white P. The above mentioned procedure was repeated for 10 times. Finally, the P/C composite was obtained after washing with a 5% NaOH aqueous solution to remove the residual P_4O_{10} . For comparison, the carbon framework alone was obtained by oxidizing red P via heating at 350°C for 2 h in air, and then washing by a 5% NaOH aqueous solution to remove the phosphorus oxides. Pure red P was prepared in the same conditions by changing the Ar flow rate to 50 sccm, and collected from the inner wall of the quartz tube.

2.2. Electrochemical characterization

The battery performance was evaluated by galvanostatic cycling of coin (CR 2032) cells with the P/C composite as the working electrode and sodium foil as the counter/reference electrode. The working electrodes were made using a typical slurry method with P/C powders, carbon black and polyvinylidene fluoride (PVDF) binder with a mass ratio of 85:5:10 in N-methyl-pyrrolidone (NMP) solvent; the mass loading of active material (P/C composite) was $\sim 2.5\text{ mg cm}^{-2}$. The electrolyte consisted of 1.0 mol L^{-1} $NaPF_6$ in an ethylene carbonate (EC)-diethyl carbonate (DEC) solution with addition of 10% fluoroethylene carbonate (FEC) in order to form a stable SEI film. [27] The electrochemical data were collected using an Arbin MSTAT battery test system within the potential range $0.01\text{--}1.5\text{ V}$ (vs. Na/Na^+) at various current densities. The specific capacity was calculated based on the total weight of phosphorus and carbon.

3. Results and discussion

The process for the fabrication of the P/C composite, featuring ultrafine red P particles (~ 10 nm) embedded in 3D carbon matrix, is schematically depicted in Fig. 1. Firstly, white P_4O_{10} particles were coated with a polymer shell of PEG in a vacuum oven at 80°C (Fig. 1a). Tens of minutes later (Fig. 1b), the mixture turned black due to dehydration and subsequent carbonization of the PEG.

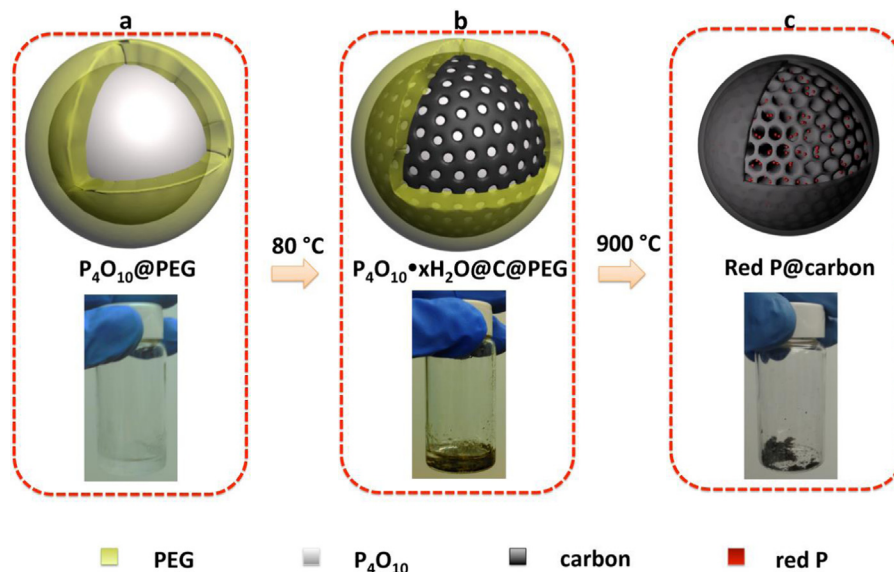


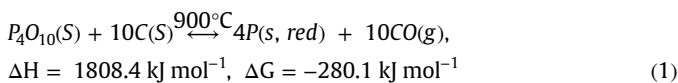
Fig. 1. Schematic and digital photographs of the synthesis procedure for the ultrafine red phosphorus particles embedded in a 3D carbon framework (P/C composite). (a) P_4O_{10} coated with PEG. (b) $P_4O_{10}\cdot xH_2O$ coated with carbon and PEG. (c) the P/C composite.

Table 1
Density and molar volume of P_4O_{10} , red P and Na_3P .

	P_4O_{10}	Red P	Na_3P
Density (g/cm^3)	2.39	2.36	1.74
Molar volume [†] (cm^3/mol (P))	59.414	13.135	57.471

[†]Molar volume calculated based on 1 mol P atom.

Meanwhile, P_4O_{10} , as a super-dehydrant, reacted with the water from PEG and polymerized to polyphosphoric acid, in the form of chain molecules with the general formula $H(HPO_3)_nOH$ [28] (Supplementary information, Fig. S2), leading to the formation of 3D channels. To achieve the final structure (Fig. 1c), PEG was further carbonized to form a 3D-structured carbon framework, while P_4O_{10} was carbothermally reduced to red P (Eq. (1)), which can occur at a temperatures higher than 743 °C. Considering the endothermic nature of this reaction ($\Delta H > 0$), the temperature was set at 900 °C, to increase the kinetic rate, as shown below:



In this final structure (Fig. 1c), the 3D carbon framework not only improves the electrical conductivity, but also provides a buffer space for the volumetric expansion of red P nanoparticles during the sodiation process. It is crucial to provide enough buffer space for accommodating the volumetric expansion. The void space is created by the volumetric shrinkage from P_4O_{10} to red P and the carbon consumption. The volumetric shrinkage ratio going from P_4O_{10} to red P is estimated to be 4.52, which matches well the volumetric expansion ratio from red P to Na_3P (4.37), as shown in Eq. (2). This suggests that there is an adequate void space for the volume expansion without cracking the 3D carbon framework (Table 1).

$$\frac{V_{mol}(P)(P_4O_{10})}{V_{mol}(P)(RP)} = 4.52 > \frac{V_{mol}(P)(Na_3P)}{V_{mol}(P)(RP)} = 4.37 \quad (2)$$

The morphology of the P/C composite was characterized by scanning electron microscopy (SEM) and transmission electron microscopy (TEM), as shown in Fig. 2. The P/C composites have a spherical shape, with a diameter ranging from 20 to 35 μm (Fig. 2a). The detailed morphology is shown in the magnified SEM image in Fig. 2b, where many pinholes with a diameter of about 100 nm can be clearly observed on the surface, suggesting the

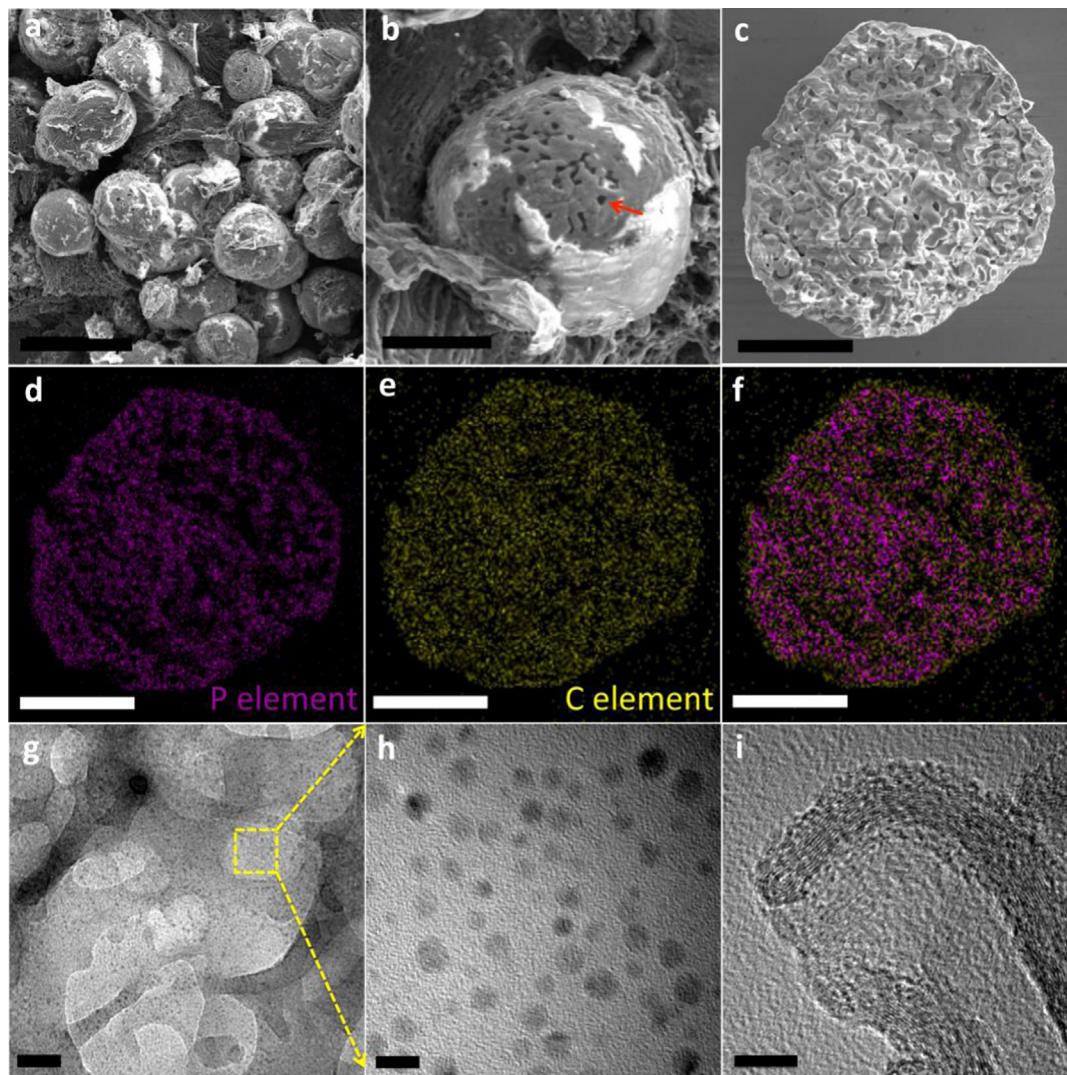


Fig. 2. SEM and TEM characterization of the P/C composite. (a) Low magnification SEM image (Scale bar, 20 μm). (b) High magnification SEM image of a single sphere (Scale bar, 10 μm). (c) SEM image of a cracked P/C sphere (Scale bar, 10 μm). The corresponding EDS elemental dot-mapping images of (d) P, (e) C elements and (f) overlay of C and P (Scale bar, 10 μm). (g) TEM image of the P/C composite (Scale bar, 100 nm). (h) Enlarged HRTEM image of the selected area in (g), with a scale bar of 10 nm. (i) HRTEM image of carbon framework (Scale bar, 10 nm).

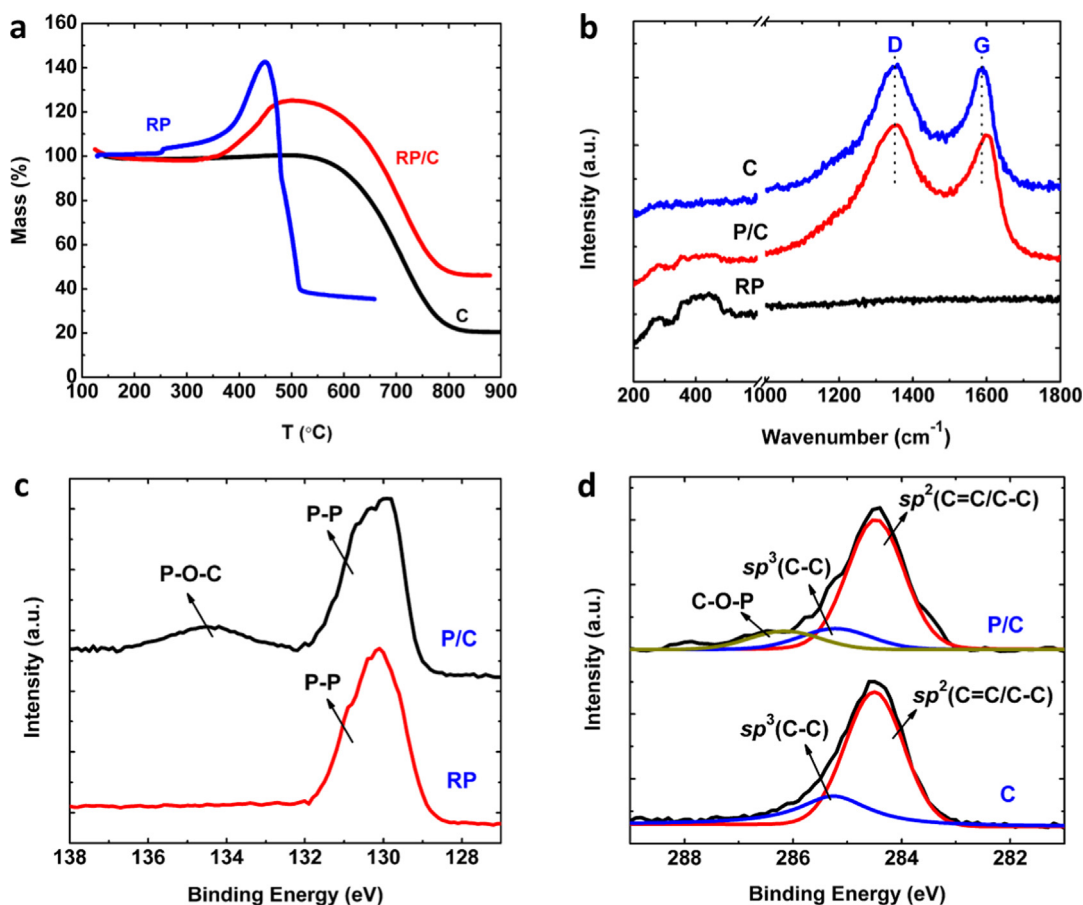


Fig. 3. Structural characterization of the P/C composite. (a) TG analysis of the P/C composite, red P and carbon framework in an air. (b) Raman spectra of the P/C composite, red P and carbon framework. (c) P2p XPS spectra of the P/C composite and red P. (d) C1s XPS spectra of the P/C composite and carbon framework. (The P/C composite, red P and carbon framework only are labeled P/C, RP and C, respectively).

presence of inner empty channels. In order to further characterize the channels, a P/C sphere was cut open by grinding to expose the 3D interconnected inner channels (Fig. 2c). The Energy dispersive spectroscopy (EDS) mapping images in Fig. 2d–f, reveal the distributions of elemental phosphorus and carbon. Carbon is uniformly dispersed (Fig. 2e), whereas phosphorus is located along the channels (Fig. 2d). As shown in the overlay EDS mapping (Fig. 2f), the border of the C dots is slightly wider than that of P, which illustrates that red P filled in the 3D channels of the carbon framework. The HRTEM image of a cracked particle (Fig. 2g) shows that the diameter of the inner channels range from several tens to hundreds of nanometers. In Fig. 2h, amorphous P clusters, with ~ 10 nm in size, are uniformly embedded in a carbon framework. Large spheres are partially coated with a thin carbon shell (Fig. 2a–b), which is less than 10 nm thick and show a certain degree of graphitization (Fig. 2i). In order to further study its hierarchical porosity, we performed nitrogen adsorption/desorption isotherm measurement for the P/C composite. The isotherms reveal a relatively high Brunauer–Emmett–Teller (BET) specific surface area (SSA) of $698.46 \text{ m}^2 \text{ g}^{-1}$ (Supplementary information, Fig. S3). The Barrett–Joyner–Halenda (BJH) pore size distribution plot indicates that the P/C composite has both micropores and mesopores (Supplementary information, Fig. S4). The large surface area and rich porosity of the hierarchical porous structure should enhance Li ion diffusivity leading to an improved high rate capability.

The structure of the P/C composite was further studied by thermogravimetric analysis (TGA), X-ray photoelectron spectroscopy (XPS) and Raman spectroscopy. Fig. 3a shows the TGA of pure red P under an atmosphere of 20% O₂ and 80% Ar. A weight

gain can be observed at 250 °C, corresponding to the oxidation of red phosphorus, followed by a sharp weight loss between 450 °C and 500 °C, due to the combustion of red phosphorus to P₂O₅ gas. The TGA of the P/C composite shows a weight increase in the 400–500 °C range, showing that the inner red-P particles were oxidized but burned. The carbon framework alone shows a dramatic mass loss in the 550–800 °C range, resulting from the oxidation of carbon and the emission of CO₂/CO gas. Similarly, the weight loss in the P/C composite above 550 °C is attributed to the oxidation of the carbon framework, not the combustion of red-P. The oxidation temperature of red-P in the P/C composite is higher than pure red-P, indicating that the red-P filled is more stable in the carbon framework. Therefore, the thermal stability of the composite is expected to be sufficient for battery applications. The P content in the composite is 36 wt% according to the TGA measurement (Supplementary information, Fig. S5).

The Raman spectrum (Fig. 3b) of the P/C composite exhibits both the characteristic G- ($\sim 1600 \text{ cm}^{-1}$) and D- ($\sim 1350 \text{ cm}^{-1}$) bands of the carbon framework and the P₇/P₉ caged feature in amorphous red-P in the 300–500 cm^{-1} region [18]. This confirms that P is present only as red P, with no signs of P₄O₁₀. In regard to carbon, the G band corresponds to the first-order scattering of the E_{2g} mode observed for sp² carbon domains, while the pronounced D band is caused by structural defects or edges that can break the symmetry and selection rules [29,30]. The intensity ratio of D band to G band (I_D/I_G) is usually used to measure the graphitization degree of carbon materials. The P/C composite has the partial-overlapped G and D bands with an I_D/I_G value of ca. 2.88, indicating that the carbon framework has a low graphitization

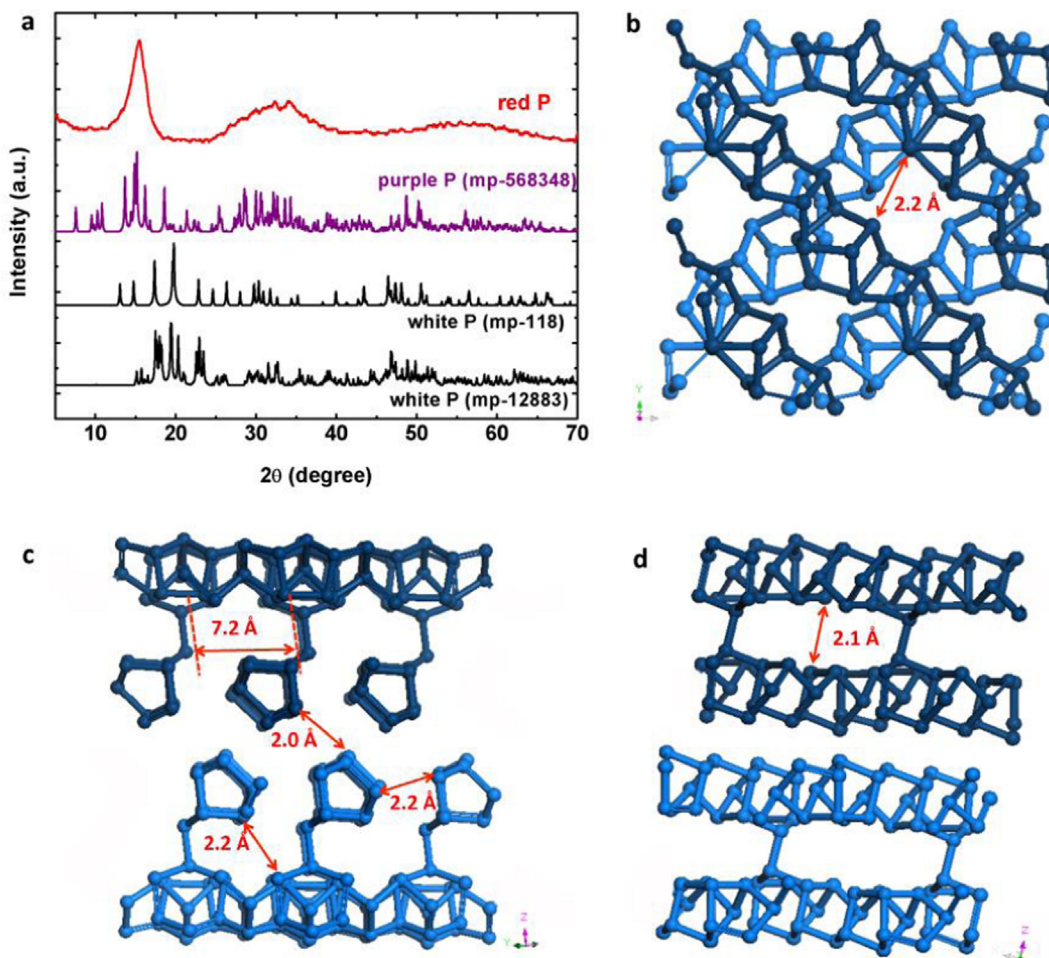


Fig. 4. Crystal structure and initial sodiation process of the as-synthesized red phosphorus. (a) The XRD spectrum of the as-synthesized red phosphorus (upper panel) and the powder diffraction files of purple P (mp-715463, IUCr) and two different phases of white P (mp-118 and mp-12883). A view of purple P crystal structure with the size-labeled channels for ion intercalation, along (b) [001], (c) [110] (d) [010] direction, respectively.

degree with disordered graphene layers. After removing red-P, the I_D/I_G value is almost the same as that in the P/C composite, but the location of the G peak shifts to a low wavenumber of 1588 cm^{-1} from 1601 cm^{-1} . Therefore, the red-shift of G band by 13 cm^{-1} is attributed to the loss of electrical contact between red-P nanoparticles and carbon framework.

The interaction between red-P nanoparticles and the carbon framework was further investigated by X-ray photoelectron spectroscopy (XPS). Two peaks centered at 130.2 eV and 134.2 eV were observed in the $P2p$ XPS spectrum of the P/C composite (Fig. 3c). The peak in the $\sim 130\text{ eV}$ region is attributed to the $P2p_{3/2}$ and $P2p_{1/2}$ from P–P bond. The relatively broad higher binding energy peak at 134.2 eV corresponds to the P–O–C bonds. In contrast, in the $P2p$ spectrum of the pure red-P, only one peak, assigned to the P–P bond, is observed at 130.2 eV. In Fig. 3d, the $C1s$ spectrum of the P/C composite can be fitted to the mainly non-oxygenated sp^2 (284.5 eV) and sp^3 (285.2 eV) carbon, and the C–O–P bond (286.1 eV). After removing red-P particles, the residual carbon framework loses the C–O–P peak at around 286.1 eV. This result indicates that O combine more strongly with P than C. As we previously mentioned, both red and black-P based anodes in SIBs, undergo a large volumetric change with breaking and regeneration of P–P bonds, leading to the loss of electrical contact of P particles with the conductive carbon materials [18,27]. Sodiation in the carbon host without breaking C–C/C=C bonds is attributed to higher bond energy of C–C/C=C bond ($346/602\text{ kJ/mol}$) than that of P–P bond (201 kJ/mol). The high bond energy of P–O–C

bonds (Supplementary information, Table S1) enables red P particles to bind strongly with the carbon framework via O atoms, and therefore helps maintain the electrical contact during electrochemical cycling.

It is known that red-P exists as an intermediate state between amorphous and crystalline, being an intermediate phase between white and purple phosphorus, and most of its properties have a range of values. In our work, the XRD spectrum (Fig. 4a) shows the red-P is close to purple-P (mp-715463, IUCr), in which Na ion can diffuse through three-dimension channels (as labeled in Fig. 4b–d) rather than only one channel in black-P [27], leading to high rate capability.

The electrochemical performance of the P/C composite and red-P were tested in a two electrode, coin-cell setup using a Na metal counter electrode, within the potential range of 1.5 to 0.01 V and at 0.2 C rate (Fig. 5a). The first discharge cycle shows two distinct electrochemical processes. The first sloping region between 1.1 V and 0.5 V corresponds partially to the insertion of Na ions into the crystalline part of red-P and partially to the irreversible formation of the SEI layer. The coulombic efficiency of the first-cycle is about 76%. The following plateau is located at 0.25 V, corresponding to the conversion reaction from red-P to Na_3P . In the following cycles, the sloping region between 1.1–0.5 V is reduced significantly, as the SEI layer has formed and the initial trapping by P has been saturated.

The carbon framework alone was also tested in the same conditions and exhibits a specific capacity of only 180 mA h g^{-1} (see

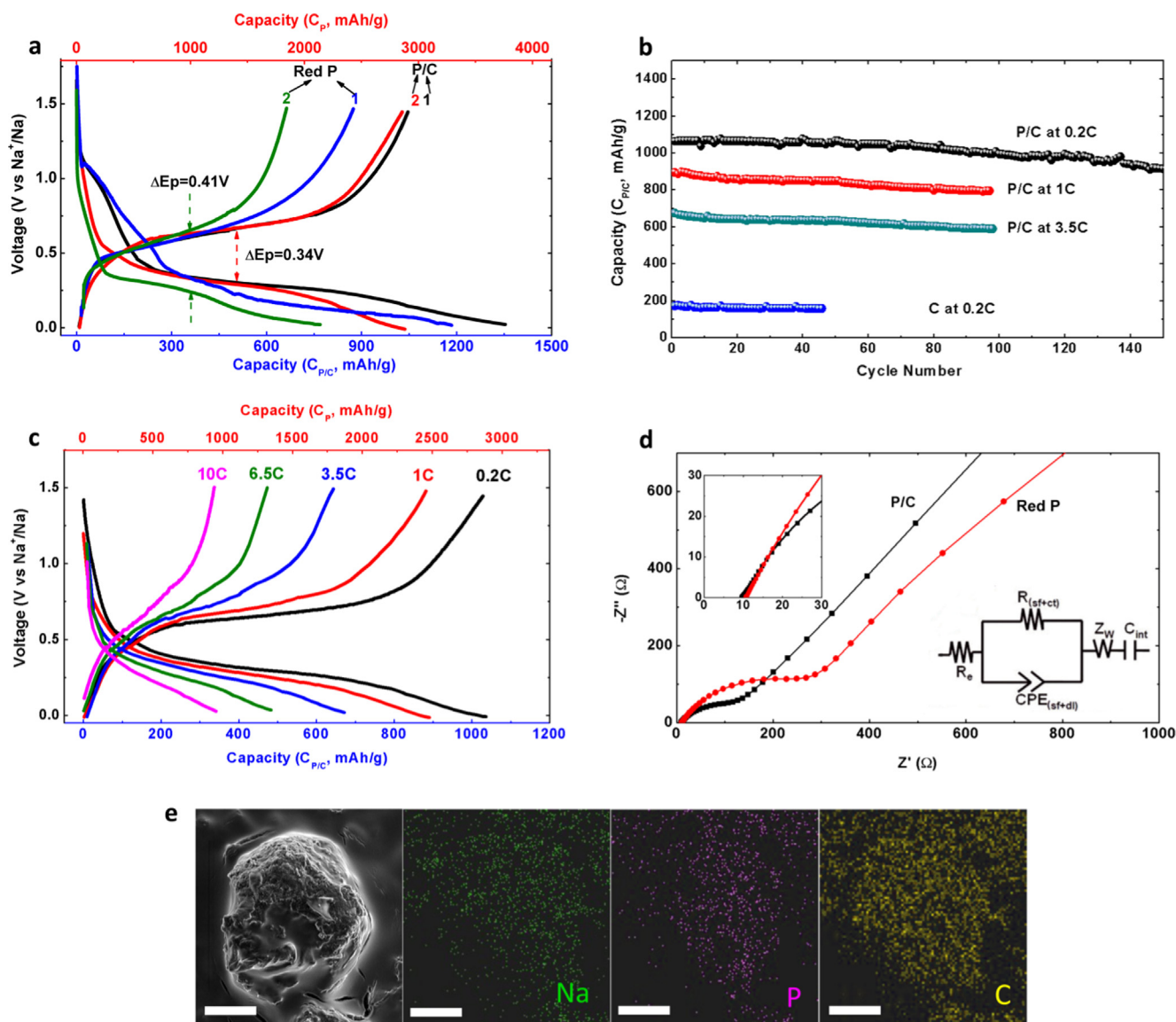


Fig. 5. Electrochemical sodium storage performance and structural evolution of the P/C composite. (a) The galvanostatic charge–discharge profiles of red P and P/C electrodes at the first two cycles between 0.01 and 1.5 V with a current density of 0.2 C. (b) the cycling performance of the carbon framework alone and the P/C composite at different current densities of 0.2 C, 1 C and 3.5 C. (c) the rate performance of the P/C electrode at various current densities from 0.2 to 10 C. C_p and $C_{P/C}$ are for the specific capacity calculated based on the weight of red P and P/C composite, respectively. (d) Nyquist plots and equivalent circuit model of P/C composite and red P electrodes after 5 cycles in discharged state. (e) SEM image of P/C sphere at full sodiated state for the 20th cycle, and the corresponding EDS elemental dot-mapping images of Na, P, and C elements (Scale bar, 10 μm).

Supplementary information, Fig. S7). Here we report the specific capacity calculated based on the total mass of red-P and carbon ($C_{P/C}$), and the weight of red P only (C_p). The comparison with the literature is summarized in Supplementary information, Table S2.

The P/C composite exhibits an initial reversible C_p specific capacity of 2853 mA h g^{-1} ($C_{P/C}$, 1027 mA h g^{-1}). After 160 cycles at 0.2 C, 920 mA h g^{-1} were still achieved (Fig. 5b), corresponding to a high capacity retention of 88%. This result demonstrates that the P–O–C bond improves the connection between the red-P nanoparticles and the carbon framework during the sodiation and desodiation processes. This performance is compared favorably to the literature studies (Supplementary information, Table S2). The electrochemical performance of a red-P electrode prepared by mixing red P, carbon black and polyvinylidene fluoride (PVDF) binder (30:60:10 wt%) was also measured, as shown in Fig. 5a. Although the first reversible discharge $C_{P/C}$ capacity of the red-P electrode was ~ 900 mA h/g , its second discharge capacity ($C_{P/C}$) decayed to 670 mA h/g , due to the poor conductivity and large

volume expansion resulting in the loss of electrical contact with the conductive carbon additive.

Due to its enhanced electrical conductivity, the P/C composite showed an outstanding rate capability (Fig. 5c). The theoretical specific capacity ($C_{P/C}$) of the P/C composite is 1049 mA h g^{-1} , which is calculated based on the theoretical specific capacity of P (2596 mA h g^{-1}) and the experimental specific capacity of C (180 mA h g^{-1}) at a low current density of 10 mA g^{-1} . A reversible capacity of 1027 mA h g^{-1} was obtained at 0.2 C (210 mA g^{-1}), reaching close to the limit. When the current density was increased to 1 C (1 A g^{-1}), it still delivers a reversible capacity of 885 mA h g^{-1} . Even at the very high rates of 3.5 C (3.6 A g^{-1}), 6.5 C (7 A g^{-1}), and 10 C (10 A g^{-1}), the electrode retains a specific capacity of 645 mA h g^{-1} , 480 mA h g^{-1} and 340 mA h g^{-1} , respectively.

To demonstrate the effectiveness of this structural design in improving the electrochemical performance, electrochemical impedance spectroscopy (EIS) was performed. Prior to the EIS tests, the cells were run for 5 cycles. The tests were then carried out

potentiostatically at 1.5 V vs Na⁺/Na in the discharged state (Fig. 5d). The Nyquist plots of both electrodes consist of a single depressed semicircle in the high-medium frequency region and an inclined line at the low frequency, respectively. The elements in the equivalent circuit include ohmic resistance of the electrolyte and cell components (R_e), surface film resistance (R_{sf}), charge-transfer resistance at the interface between the electrode and electrolyte (R_{ct}), a constant phase element (CPE_i) (surface film (sf), double layer (dl)) used instead of pure capacitance due to the depressed semicircle, [18] Warburg impedance (Z_w), and intercalation capacitance (C_{int}). According to the fitting with this equivalent circuit, the value of R_e is 8–12 Ω for the both samples, indicating that the cells have been properly fabricated and tested in the same condition. Due to the single semicircle observed, the impedance can be ascribed to the combination of the surface film and charge-transfer resistance $R(sf+ct)$. The fitting parameter of $R(sf+ct)$ is much lower for the P/C electrode (176.4 Ω) compared to the red P (391.6 Ω), which means that the P/C electrode has a faster charge-transfer process than the red-P electrode.

The structural evolution of the P/C composite during the electrochemical process was investigated by SEM (Fig. 5e). The spherical structure integrity is maintained without cracking after 20 sodiation/desodiation cycles. We attribute the good sodium storage performance of the P/C composite to its 3D porous architecture. The channels in the carbon framework not only function as an electrical highway in which sodium ions and electrolyte can be transported, but also give a buffer space allowing the P particles to expand.

4. Conclusions

In conclusion, we report a facile synthesis method to fabricate a 3D-structured P/C composite starting from P₄O₁₀, which performs not only as the template to fabricate the 3D channels by dehydrating PEG, but also as P source to produce red-P by carbothermic reduction. Ultrafine red-P nanoparticles accommodate the large stress without cracking, and decrease the diffusion length, as well as the improved conductivity by connecting to carbon framework via P–O–C bonds. The P/C composite as anode material for SIBs delivers a capacity of $C_{P/C}$ at 920 mA h g⁻¹ at 160th cycle with a capacity retention of 88%. Moreover, this P/C composite is low cost and stable in air and is expected to be a scalable anode material for the next generation of SIBs.

Acknowledgements

This work was supported by the Department of Energy, Office of Basic Energy Sciences, Division of Materials Sciences and Engineering, under Contract DE-AC02-76SF00515.

Appendix A. Supplementary material

Supplementary data associated with this article can be found in the online version at <http://dx.doi.org/10.1016/j.ensm.2016.04.003>.

References

- Li Y, Mu L, Hu Y-S, Li H, Chen L, Huang X. Pitch-derived amorphous carbon as high performance anode for sodium-ion batteries. *Energy Storage Mater.* 2016;2:139–145.
- Zhang S-W, Lv W, Luo C, You C-H, Zhang J, Pan Z-Z, Kang F-Y, Yang Q-H. Commercial carbon molecular sieves as a high performance anode for sodium-ion batteries. *Energy Storage Mater.* 2016;3:18–23.
- Luo W, Shen F, Bommier C, Zhu H, Ji X, Hu L. Na-ion battery anodes: materials and electrochemistry. *Acc. Chem. Res.* 2016;49:231–240.
- Slater MD, Kim D, Lee E, Johnson CS. Sodium-ion batteries. *Adv. Funct. Mater.* 2013;23:947–958.
- Tarascon JM, Armand M. Issues and challenges facing rechargeable lithium batteries. *Nature* 2001;414:359–367.
- Barpanda P, Oyama G, Nishimura SI, Chung SC, Yamada A. A 3.8-V earth-abundant sodium battery electrode. *Nat. Commun.* 2014;5:4358.
- Ellis BL, Makahnouk WRM, Makimura Y, Toghiani K, Nazar LF. A multifunctional 3.5 V iron-based phosphate cathode for rechargeable batteries. *Nat. Mater.* 2007;6:749–753.
- Lee HW, Wang RY, Pasta M, Lee SW, Liu N, Cui Y. Manganese hexacyanomanganate open framework as a high-capacity positive electrode material for sodium-ion batteries. *Nat. Commun.* 2014;5:5280.
- Chan CK, Peng H, Liu G, McIlwrath K, Zhang XF, Huggins RA, Cui Y. High-performance lithium battery anodes using silicon nanowires. *Nat. Nanotechnol.* 2008;3:31–35.
- Chevrier VL, Ceder G. Challenges for Na-ion negative electrodes. *J. Electrochem. Soc.* 2011;158:A1011–A1014.
- Komaba S, Murata W, Ishikawa T, Yabuuchi N, Ozeki T, Nakayama T, Ogata A, Gotoh K, Fujiwara K. Electrochemical Na insertion and solid electrolyte interphase for hard-carbon electrodes and application to Na-ion batteries. *Adv. Funct. Mater.* 2011;21:3859–3867.
- Li WJ, Chou SL, Wang JZ, Liu HK, Dou SX. Simply mixed commercial red phosphorus and carbon nanotube composite with exceptionally reversible sodium-ion storage. *Nano Lett.* 2013;13:5480–5484.
- Baggetto L, Keum JK, Browning JF, Veith GM. Germanium as negative electrode material for sodium-ion batteries. *Electrochem. Commun.* 2013;34:41–44.
- Zhu H, Jia Z, Chen Y, Weadock N, Wan J, Vaaland O, Han X, Li T, Hu L. Tin anode for sodium-ion batteries using natural wood fiber as a mechanical buffer and electrolyte reservoir. *Nano Lett.* 2013;13:3093–3100.
- Jow TR, Shacklette LW, Maxfield M, Vernick D. The role of conductive polymers in alkali-metal secondary electrodes. *J. Electrochem. Soc.* 1987;134:1730–1733.
- Darwiche A, Marino C, Sougrati MT, Fraisse B, Stievano L, Monconduit L. Better cycling performances of bulk sb in Na-ion batteries compared to Li-ion systems: an unexpected electrochemical mechanism. *J. Am. Chem. Soc.* 2012;134:20805–20811.
- Extance P, Elliott SR. Pressure dependence of the electrical conductivity of amorphous red phosphorus. *Philos. Mag. B* 1981;43:469–483.
- Sun J, Zheng G, Lee HW, Liu N, Wang H, Yao H, Yang W, Cui Y. Formation of stable phosphorus–carbon bond for enhanced performance in black phosphorus nanoparticle-graphite composite battery anodes. *Nano Lett.* 2014;14:4573–4580.
- Qian J, Wu X, Cao Y, Ai X, Yang H. High capacity and rate capability of amorphous phosphorus for sodium ion batteries. *Angew. Chem. Int. Ed.* 2013;52:4633–4636.
- Kim Y, Park Y, Choi A, Choi NS, Kim J, Lee J, Ryu JH, Oh SM, Lee KT. An amorphous red phosphorus/carbon composite as a promising anode material for sodium ion batteries. *Adv. Mater.* 2013;25:3045–3049.
- Qian J, Qiao D, Ai X, Cao Y, Yang H. High capacity and rate capability of amorphous phosphorus for sodium ion batteries. *Chem. Commun.* 2012;48:8931–8933.
- Li W, Chou S, Wang J, Liu H, Dou S. Simply mixed commercial red phosphorus and carbon nanotube composite with exceptionally reversible sodium-ion storage. *Nano Lett.* 2013;13:5480–5484.
- Zhu Y, Wen Y, Fan X, Gao T, Han F, Luo C, Liou S, Wang C. Red phosphorus-single-walled carbon nanotube composite as a superior anode for sodium ion batteries. *ACS Nano* 2015;9:3254–3264.
- Song J, Yu Z, Gordin ML, Hu S, Yi R, Tang D, Walter T, Regula M, Choi D, Li X, Manivannan A, Wang D. Chemically bonded phosphorus/graphene hybrid as a high performance anode for sodium-ion batteries. *Nano Lett.* 2014;14:6329–6335.
- Wu H, Chan G, Choi JW, Ryu I, Yao Y, McDowell MT, Lee SW, Jackson A, Yang Y, Hu L, Cui Y. Stable cycling of double-walled silicon nanotube battery anodes through solid-electrolyte interphase control. *Nat. Nanotechnol.* 2012;7:310–315.
- Liu N, Lu Z, Zhao J, McDowell MT, Lee HW, Zhao W, Cui Y. A pomegranate-inspired nanoscale design for large-volume-change lithium battery anodes. *Nat. Nanotechnol.* 2014;9:187–192.
- Sun J, Lee HW, Pasta M, Yuan H, Zheng G, Sun Y, Li Y, Cui Y. A phosphorene-graphene hybrid material as a high-capacity anode for sodium-ion batteries. *Nat. Nanotechnol.* 2015;10:980–985.
- D.E.C. Corbridge, Phosphorus Chemistry Biochemistry and Technology, sixth ed., 119, 2013.
- Li G, Li Y, Liu H, Guo Y, Li Y, Zhu D. Architecture of graphdiyne nanoscale films. *Chem. Commun.* 2010;46:3256–3258.
- Sun J, Liu H, Chen Xu, Evans DG, Yang W, Duan X. Synthesis of graphene nanosheets with good control over the number of layers within the two-dimensional galleries of layered double hydroxides. *Chem. Commun.* 2012;48:8126–8128.